Earth and Planetary Science Letters 460 (2017) 152–163

Contents lists available at ScienceDirect

Earth and Planetary Science Letters

www.elsevier.com/locate/epsl

Miocene development of alpine glacial relief in the Patagonian Andes, as revealed by low-temperature thermochronometry

Elizabeth C. Christeleit [a,*], Mark T. Brandon [a], David L. Shuster [b,c]

[a] Yale University, New Haven, CT, United States
[b] UC Berkeley, Berkeley, CA, United States
[c] Berkeley Geochronology Center, Berkeley, CA, United States

ARTICLE INFO

Article history:
Received 9 May 2016
Received in revised form 8 December 2016
Accepted 12 December 2016
Available online 27 December 2016
Editor: A. Yin

Keywords:
apatite
(U–Th)/He thermochronometry
^{4}He/^{3}He
Patagonian Andes
glacial erosion
landscape evolution

ABSTRACT

Apatite thermochronometry and synthetic maps of ages and rates for thermochronometric data are used to estimate the timing of incision of valley relief in the Andes. Central Patagonia offers a unique location to study the feedbacks between long-term climate, topography, and erosion due to the high relief and well-resolved mid-latitude glacial history. New apatite (U–Th)/He ages from two vertical transects and two ^{4}He/^{3}He release spectra in the fjord network around 47°S reveal fast cooling (15–30 °C/Ma) from ~10 to 5 Ma. Samples currently at the surface cooled below ~35 °C by ~5 Ma, indicating slow cooling and little erosion in those regions since 5 Ma. We show that these very low-temperature thermochronometric data are useful indicators of changes in topography, and insensitive to deep thermal processes, such as migration of the Chile triple junction. Map-based predictions of the thermochronometric signatures of disparate topographic scenarios show the distribution of sample data necessary to resolve the timing of relief change. Comparisons to predicted cooling ages and rates indicate that our new apatite He data are most consistent with a pulse of early glacial incision, with much of the observed valley relief in Patagonia carved between 10 and 5 Ma. Early onset of glaciation in Patagonia is supported by glacial till with bracketing ages of 7.4 and 5 Ma. We therefore conclude that the observed thermochronometric signal of fast cooling from 10 to 5 Ma is likely due to an increase in valley relief coinciding with these early glaciations in the Andes. In other glaciated areas at lower latitudes, studies have found a dramatic increase in valley relief at ~1 Ma. This timing has generated the idea that incision of glacial valleys may be related to the mid-Pleistocene transition, when the global glacial cycle changed from 40 to 100 ka periods. Our results from a higher latitude indicate an alternative, that glacial valleys incised rapidly after the onset of alpine glaciation.

© 2016 Elsevier B.V. All rights reserved.

1. Introduction

Deep valleys and fjords, with relief of 1 to 2 km, are common features of continental landscapes at latitudes poleward of 48°N, and 42°S. However, it is easy to overlook the extreme relief associated with these features, given that they are commonly concealed by water, ice, and sediment. Glacial erosion is unlike fluvial erosion, in that the long profile of the valley can cut well below base level at the outlet. This leads to glacially cut valleys that are "overdeepened", where the middle reach is significantly deeper than sea level and the seaward outlet. This situation is well known for fjords and glacially carved lakes (inland fjords). For example, the deepest fjords in the world, Skelton Inlet in Antarctica, and Fjord Messier in southern Chile, extend to 1933 m, and 1468 m, respectively, below sea level.

Overdeepened valleys were recognized long ago as a geomorphic feature diagnostic of glacial erosion (e.g. Ramsay, 1862). Notable research over the last several decades includes process-based studies of their formation (e.g., Hooke, 1991; Alley et al., 2003; Kessler et al., 2008; Headley et al., 2012), and geologic studies of fjord morphology and post-glacial fill (e.g., Montgomery, 2002; Glasser and Ghiglione, 2009; Dowdeswell and Vasquez, 2013). How glacial valleys and fjords develop over time, and what role climate and tectonics play in controlling the development of extreme valley relief remains unclear. Here, we focus on quantifying the timing and rate of glacial valley formation in southern Chile.

Our understanding of glacial landscape development is limited by our ability to reconstruct pre-glacial topography and glacial landforms through time. The low temperature sensitivity of the

* Corresponding author.
E-mail address: elizabeth.christeleit@yale.edu (E.C. Christeleit).

http://dx.doi.org/10.1016/j.epsl.2016.12.019
0012-821X/© 2016 Elsevier B.V. All rights reserved.

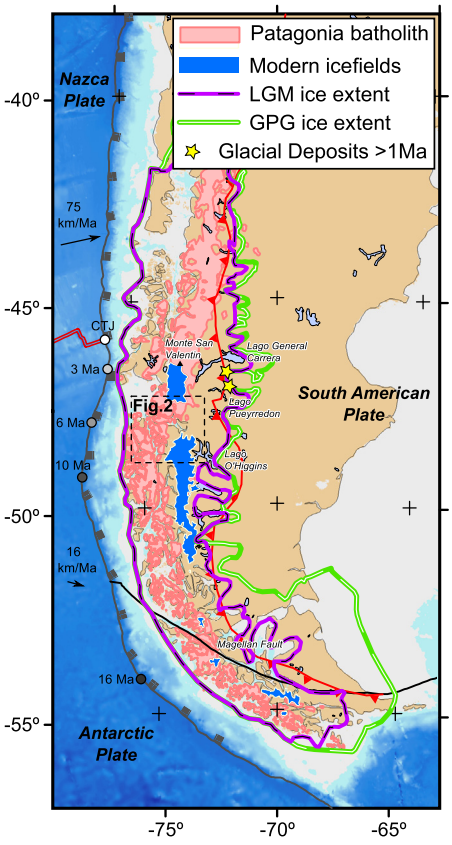

Fig. 1. Map of Patagonia with extent of modern and Last Glacial Maximum (LGM, 20 ka) glaciations, and the Greatest Patagonian Glaciation (GPG, ~1.2 to 1.0 Ma). The yellow stars show the location of older glacial deposits (~6 Ma and 3.4 Ma). The Cretaceous–Paleogene Patagonian Batholith (pink) underlies the core of the Patagonian Andes. The Nazca, South American, and Antarctic plates meet at the Chile triple junction, located at ~46.5°S. The circles and ages show the migration path of the triple junction along the Chile trench (Breitsprecher and Thorkelson, 2009). (For interpretation of the colors in this figure, the reader is referred to the web version of this article.)

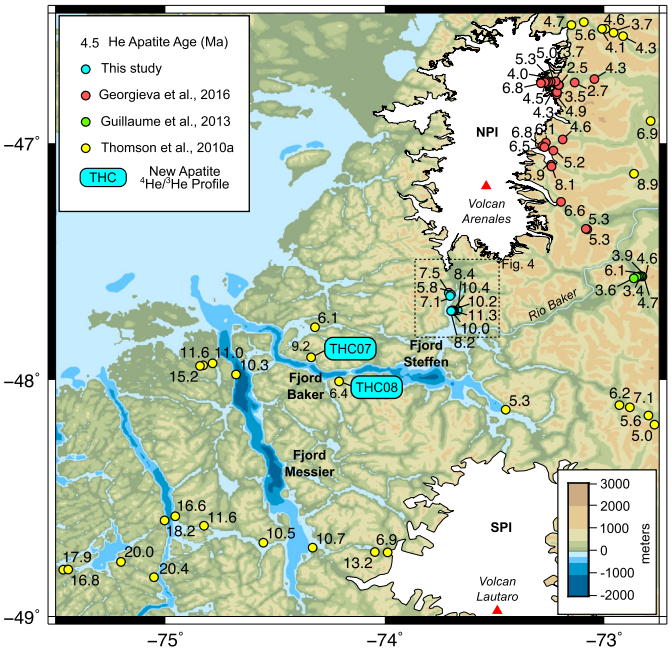

Fig. 2. Topography and bathymetry of our study area with existing and new apatite He ages (our study; Thomson et al., 2010a; Guillaume et al., 2013; Georgieva et al., 2016). Our study provides new He apatite cooling ages from two vertical transects in Fjord Steffen and two $^4He/^3He$ analyses from Fjord Baker. Grid resolution for elevation and bathymetry is better than 925 m grid spacing (SRTM30 Plus v6.0).

apatite (U–Th–Sm)/He and $^4He/^3He$ thermochronometric systems make these methods useful for quantifying rates and timing of landscape change, e.g., in the evolution of fluvial valleys in the Northern Andes and the Grand Canyon (Schildgen et al., 2010; Flowers and Farley, 2012, respectively), and glacial valleys in the Coast Mountains of British Columbia, the Fiordland of New Zealand, and the Swiss Alps (Shuster et al., 2005, 2011; Valla et al., 2011, respectively). In glacial landscapes, where geologic markers of landscape change are eroded by subsequent glaciations, low-temperature thermochronometry offers perhaps the only method to measure the evolution of valley incision on a geologic time scale.

Southern Chile (~47°S) preserves a relatively long history of alpine glaciations, where the earliest known glacial till lies between two basalt flows, with ages of 7.38 ± 0.05 and 5.04 ± 0.04 Ma (Fig. 1; Mercer and Sutter, 1982; Ton-That et al., 1999). Mountain building and glacial erosion have resulted in dramatic modern bedrock relief, bounded by the ~4 km summit of Monte San Valentin to ~1.5 km below sea level at the deepest part of Fjord Messier. Northward migration of the Chile triple junction and associated oblique subduction of the Chile ridge (Cande and Leslie, 1986) is thought to play a dominant role in the cooling and heating history of upper crustal bedrock, and relief development in the region (Haschke et al., 2006; Guillaume et al., 2013; Georgieva et al., 2016). We show here, using thermal modeling, that the triple junction has had little influence on temperatures in the shallow crust (<3 km depth). As a result, for this study area, low-temperature thermochronometry records the thermal signal of erosion and relief change.

In this contribution, we explore various end-member hypotheses for the timing of glacial incision in southern Chile and develop a method to study the thermochronometric signature of the formation of valley relief over geologic timescales. Our method illustrates the ability of He apatite methods to discriminate between disparate topographic histories. We compare predicted cooling ages and rates for several end-member hypotheses of valley incision to our observed apatite (U–Th–Sm)/He and $^4He/^3He$ data from the fjords in central Patagonia (~47°S). The new data require that glacial incision in southern Chile occurred between 10 and 5 Ma, coinciding with previously recognized early glaciations in the region (Mercer and Sutter, 1982; Ton-That et al., 1999). Our results highlight the importance of relief formation in the long-term evolution of glacial landscapes and suggest that glacial erosion proceeds rapidly after the onset of glaciation.

2. Central Patagonian Andes

2.1. Geomorphic setting

There is a dense network of fjords and glacially carved lakes in southern Chile, which are deep depressions fully surrounded by bedrock on all sides (Fig. 2). Fjord Messier is the most extreme example, with a maximum depth of 1468 m below sea level (Araya-Vergara, 2008), and subaerial topography that locally rises to ~500 m above sea level. The relief and width of this valley is 2000 m and 24 km, respectively. For comparison, the Grand Canyon in Arizona has an average valley relief of 1600 m and an average width of 16 km. The seaward ends of the fjords terminate abruptly at the inside limit of the continental shelf, with terminal sills that rise to within 100 m of modern sea level. The lakes in the region are all overdeepened. The most extreme are Lago O'Higgins/San Martín, Lago General Carrera/Buenos Aires, and Lago Pueyrredón/Cochrane, which are cut to depths of 586 m, 313 m, and 307 m, respectively, below sea level (Fig. 1). All of the rivers

in the area are underfit, in that they are much too small to have cut their valleys. The largest fluvial system, the Rio Baker (Fig. 2), presently cuts across the entire width of the Andes, flowing from Lago Buenos Aires/General Carrera on the east of the Andes, to the Pacific Ocean on the west side. Its course seems largely determined by interconnected glacial valleys.

At present, the North and South Patagonian icefields (NPI and SPI) collectively represent the third largest glacial mass in the world (21,000 km^2 area; Fig. 1). The distribution of Quaternary moraines indicates that, during glacial epochs, the extent of ice was about 25 times larger than the modern extent. These glacial maxima formed recurring ice caps, which covered the Patagonian Andes from 36°S to 55°S, with typical widths of ~100–300 km (Fig. 1; Caldenius, 1932; Clapperton, 1993). While there is no independent data for when glaciation began in Patagonia, the earliest known glacial tills in the region are bracketed by basalt flows of 7.38 ± 0.05 and 5.04 ± 0.04 Ma, and 3.44 ± 0.1 and 3.32 ± 0.1 Ma (yellow stars in Fig. 1; Mercer and Sutter, 1982; Ton-That et al., 1999; Guivel et al., 2006). These deposits contain granitic cobbles sourced from the Patagonian batholith 100 km to the west (Fig. 1; Mercer and Sutter, 1982), suggesting that these early glaciations also formed large ice caps. The modern equilibrium line altitude (ELA) of glaciers in the North Patagonian icefield is estimated to be between ~1000 to 1300 m (Rivera et al., 2007). Estimates of the paleo-ELA are complicated by the fact that during glacial epochs, a lowering of temperature is accompanied by a northward migration of precipitation belts (for estimates see discussion in Hulton et al., 1994).

2.2. Tectonic setting

The high topography of the Patagonian Andes was formed by back-arc thrusting and folding, starting at ~30 Ma (see Ramos and Ghiglione, 2008 and references within). Blisniuk et al. (2005) estimate that the range reached its present height (summits higher than 1.5 km) by ~16 Ma. The eastern frontal thrust faults became inactive by 8 Ma (Ramos, 1989), which suggests that surface uplift by tectonic thickening has been insignificant since that time. Neotectonic activity on dextral strike–slip faults has been identified in the Liquine–Ofqui Fault Zone northwest of the NPI and on the eastern flank of the NPI (Cachet Fault; Georgieva et al., 2016). Georgieva et al. (2016) also identify normal faults in the Exploradores Valley adjacent to Monte San Valentin, and at El Salton along the Rio Baker. Interpretation of low-temperature thermochronometric data suggests that the Cachet Fault and associated normal faults became active in the last 2–3 Ma (Georgieva et al., 2016).

The study area includes two active volcanoes, Arenales and Lautaro (Fig. 2). Both have erupted through the North and South Patagonian ice fields, and have formed small stratocones, built directly on old bedrock. They are otherwise dwarfed by the bedrock topography. The highest point in the landscape, Monte San Valentin (4058 m), is entirely underlain by Cretaceous and Paleogene granites and older metamorphic rocks.

2.3. Chile triple junction

Plate reorganization in the middle Miocene led to the formation of the Chile triple junction along the South American trench at 54°S at ~20 Ma (Cande and Leslie, 1986; Breitsprecher and Thorkelson, 2009). This junction migrated northward to its present position at 46.5°S (Fig. 1) by episodic subduction of Antarctic-Nazca spreading ridge segments (Cande and Leslie, 1986). Discussion has focused on the influence of the triple junction on surface uplift, heating, and deformation in the overriding plate (e.g., Cande and Leslie, 1986; Ramos and Ghiglione, 2008; Guillaume et al., 2013; Braun et al., 2013). For example, Haschke et al. (2006) and Guillaume et al. (2013) interpret apatite He and fission-track data from 47.5°S to 45.3°S as evidence for a pulse of crustal heating from 12 to 5 Ma. In this scenario, topographic uplift and an associated increase in surface erosion rates preceded the arrival of the triple junction offshore, because the triple junction was south of 47°S until ~6 Ma (Fig. 1).

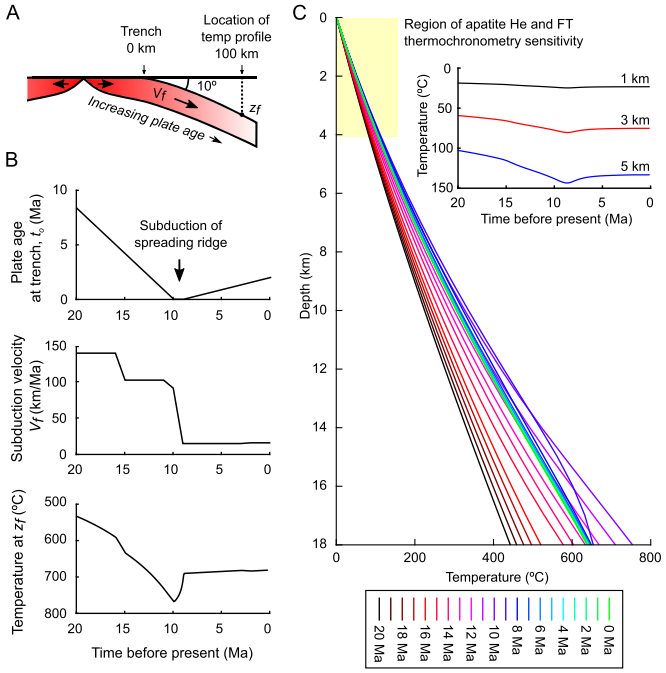

Fig. 3. One-dimensional model of the thermal influence of the passage of the Chile triple junction beneath our study area over the last 20 Ma. The vertical temperature profile was calculated 100 km inland from the Chile trench at 47.5°S. (a) Simplified representation of the subduction zone. V_f is the downgoing plate velocity, and z_f is the local depth to the subduction thrust. (b) Model inputs: plate age t_o at the trench at 47.5°S from 20 to 0 Ma (Cande and Leslie, 1986); subduction velocity V_f through time; temperature at z_f on the subduction thrust from 20 to 0 Ma. Prior to 10 Ma, the Nazca plate was subducted at a trench orthogonal rate of >100 km/Ma. The age of the subducted oceanic lithosphere became progressively younger until the Antarctic–Nazca spreading ridge was subducted from ~10–8 Ma (Cande and Leslie, 1986; Breitsprecher and Thorkelson, 2009). Since 8 Ma, the Antarctic plate has been subducted at an orthogonal rate of ~20 km/Ma (Breitsprecher and Thorkelson, 2009). (c) Vertical temperature profile through time. The inset shows the modeled temperature at a depth of 1, 3, and 5 km from 20 to 0 Ma.

To understand the influence of a thermal perturbation caused by subduction of progressively younger oceanic lithosphere and the Chile ridge, we perform a 1D calculation of the thermal field in the upper plate using a model developed by Molnar and England (1995) (Fig. 3; see Appendix A in the supplementary material for details). Fig. 3c shows the temperature profile through the upper plate at a fixed point on the upper plate, 100 km from the trench. The temperature profile is modeled over a 20 Ma interval. Over this time interval, progressively younger oceanic crust was subducted until the Chile ridge itself is at the trench at 8 Ma, followed by a gradual increase in plate age at the trench (Fig. 3b).

Two important conclusions can be drawn from Fig. 3. The first concerns the evolution of upper-plate heating. Fig. 3 shows gradual heating and subsequent cooling over a duration of 15 Ma. Regional heating caused by migration of the triple junction is protracted in time, and does not produce a pulse of heating, as suggested by Guillaume et al. (2013). The reason is that heating of the upper plate is not solely related to the subduction of the Chile ridge, but also to the young age of the downgoing lithosphere adjacent to the ridge. The second conclusion concerns the influence of ridge subduction on temperatures in the upper few kilometers of the

crust (∼2.5 km), which is relevant to apatite He thermochronometry. Fig. 3 shows that a temperature increase of ∼300 °C on the subduction thrust at 18 km depth causes a maximum change in temperature ∼20 °C at a depth of 3 km. The overall conclusion is that a migrating triple junction has little influence on the shallow temperature field, as relevant to the apatite He system. In this study region, we therefore assume that low-temperature thermochronometric data are insensitive to heating and cooling caused by migration and subduction of the Chile ridge. Instead, the apatite He thermochronometric system is most sensitive to changes in erosion and topographic relief at the landscape surface.

2.4. Glacial erosion rates in southern Chile

At present, there are apatite He and fission-track ages for samples from about 300 localities along the 2000 km length of the Patagonian Andes (a limited number of locations and ages are shown in Fig. 2, see Thomson et al., 2010a and Herman and Brandon, 2015 for compilation). These ages collectively provide a regional framework for our understanding of glacial erosion in southern Chile. Note that throughout this paper, we use the term *exhumation* to describe the motion of a bedrock sample towards the topographic surface, and *erosion* to describe the removal of rock at the surface. Thomson et al. (2010a) argue that samples from the northern half of the Patagonian Andes saw a clear increase in exhumation rates over the last 6 Ma, whereas those from the southern half saw no increase in exhumation rates. They proposed that more southern latitudes should have favored cold-based glaciation, which is less erosive than warm-based glaciation (Hallet et al., 1996). Using a full numerical analysis of the dataset, Herman and Brandon (2015) show that, prior to 2 Ma, exhumation was everywhere slow in the Patagonian Andes, with rates of 0.2 to 0.3 km/Ma. Since 2 Ma, a "hot spot" developed between 42° to 46°S latitude, with exhumation rates averaging 0.8 to 1.5 km/Ma. For the Patagonian Andes south of 46°S, exhumation rates remained low, at the same rate of 0.2 to 0.3 km/Ma, including the area adjacent to Chile triple junction, located at 46.5°S. We emphasize that the regional thermochronometric data and the numerical solution provide only a smoothed view of the exhumation history of the region. Long-wavelength features (>∼100 km) are well resolved, but local features, such as glacial valleys, which were formed by locally fast erosion at the surface, are not resolved.

3. Apatite He thermochronometry

Erosion at Earth's surface causes the underlying bedrock to cool as it moves upward through the subsurface thermal field. Thermochronometry provides quantitative constraints on that cooling history. The (U–Th–Sm)/He thermochronometric system in apatite is based on decay of isotopes of U, Th, and Sm and the accumulation of the daughter ^{4}He inside of the apatite host crystal (Farley, 2002; Ehlers and Farley, 2003). Retention of ^{4}He is controlled by thermally-activated diffusion, with a closure temperature between ∼50–100 °C for a cooling rate of 10 °C/Ma (Shuster et al., 2006). The apatite He system therefore has a very shallow closure depth, ∼2 km, which means that it is uniquely able to measure exhumation rates over short timescales (∼1 Ma) and to resolve the spatial pattern of exhumation, which is essential for determining when large valleys were cut.

Together, apatite He ages and ^{4}He/^{3}He release spectra provide two related datasets that constrain cooling histories on different timescales and at different resolutions (e.g. Valla et al., 2011). An apatite (U–Th–Sm)/He age ("He age") provides information on the time-temperature history, but requires additional information about the cooling rate and local geothermal gradient to constrain the timing of cooling through a particular temperature threshold. A suite of He ages along a vertical transect shows the present spatial distribution of cooling ages as a function of elevation. The age-elevation relationship is often interpreted in terms of when the individual sampled points passed through the closure isotherm at depth, yielding an average exhumation rate over the time interval of the oldest to youngest He age. The rate of subsequent exhumation can be estimated by the He apatite age of bedrock currently at the upper thermal boundary, approximated by the local mean elevation of the landscape ("time-of-flight" in McPhillips and Brandon, 2010). For example, consider a scenario with a closure depth of ∼2 km below the mean elevation and a He age of 6 Ma at the mean elevation. The sample at mean elevation moved vertically ∼2 km over the interval from 6 to 0 Ma, indicating an average exhumation rate of ∼0.3 km/Ma over this period.

Apatite ^{4}He/^{3}He data extend the resolution of the He system to much lower temperatures, by estimating the cooling history of an individual sample over the interval ∼80 to 35 °C (Shuster et al., 2004; Shuster and Farley, 2004, 2005). For this analysis, an apatite crystal is irradiated with ∼220 MeV protons to produce a spatially uniform distribution of spallation ^{3}He, which serves as a reference for the ^{4}He analysis. Both radiogenic ^{4}He and the proton-induced ^{3}He are sequentially degassed from individual apatite crystals, which initially diffuses ^{4}He from the rim, given the short diffusion path, and eventually from the core, given the longer diffusion path. The measured ^{4}He/^{3}He ratio release spectrum thus estimates the radial distribution of ^{4}He in the crystal that resulted from open-system behavior during ^{4}He accumulation. This information can then be used to constrain the sample's permissible cooling history between ∼80 to 35 °C starting at some time in the past and ending at the present (Shuster et al., 2011).

4. Thermochronometric data from the Patagonian fjords

In this study, we collected and analyzed samples from two vertical transects in Fjord Steffen (Table 1, Fig. 4) and analyzed previously collected samples (Thomson et al., 2010a) from Fjord Baker for apatite ^{4}He/^{3}He release spectra (locations of samples THC07 and THC08 are shown in Fig. 2; results of ^{4}He/^{3}He analysis are shown in Fig. 5 and in the supplementary material). Samples sites were selected because they are adjacent to the fjords, where valley relief is greatest. Apatite He ages and ^{4}He/^{3}He release spectra were measured in the Noble Gas Thermochronometry Lab of the Berkeley Geochronology Center. Well-formed, inclusion-free apatite crystals were selected with a polarizing-light stereo microscope. For (U–Th–Sm)/He analyses, each individual crystal was degassed by laser heating and the ^{4}He concentration was measured using isotope dilution and quadrupole mass spectrometry (see Tremblay et al., 2015 for analytical details). U, Th, and Sm concentrations were measured by isotope dilution using an ICP-MS.

Fig. 4 shows the mean, standard error, and associated young concordant crystal ages for the replicated samples from Fjord Steffen (see supplementary material for full results). The apatite He ages are largely clustered between 6 and 12 Ma. The two elevation transects in Fjord Steffen show similar age-elevation trends (Fig. 4, red and blue dashed lines), indicating fast exhumation (∼1.0 km/Ma) from 10 to 6 Ma. The mean cooling age of the two profiles observed at the mean elevation (∼8 Ma at ∼600 m) indicates slower exhumation, ∼0.3 km/Ma, from 6 to 0 Ma (based on an estimated closure depth of 2 km below sea level). The trend lines of the two age-elevation plots are offset by ∼2.5 Ma. Georgieva et al. (2016) find a similar offset of He ages in two vertical transects on the eastern slope of the NPI, which they attribute to differential tectonic uplift, post-dating the closure of the apatite He system of the youngest samples. There are no observed

Table 1
Apatite (U–Th)/He sample data and mean ages.

Sample	Latitude (°S)	Longitude (°W)	Elevation (m)	Mean age (Ma)	SE (Ma)
Fjord Steffen Northern Transect					
FS01	47.62830	73.71111	1013	*not replicated*	
FS02	47.63228	73.70897	842	7.5	0.97
FS04	47.63371	73.70287	534	*not replicated*	
FS06	47.63965	73.69865	251	5.8	0.21
FS17	47.64607	73.70287	105	7.14	0.81
Fjord Steffen Southern Transect					
FS08	47.70565	73.66784	1175	8.4	0.99
FS10	47.70781	73.67954	872	*not replicated*	
FS11	47.70767	73.68395	709	10.44	3.78
FS12	47.70814	73.68685	573	10.21	0.43
FS13	47.70799	73.68935	417	11.29	0.92
FS14	47.70662	73.69276	267	10	0.71
FS15	47.70860	73.69539	128	*not replicated*	
FS16	47.70908	73.69784	0	8.23	0.29

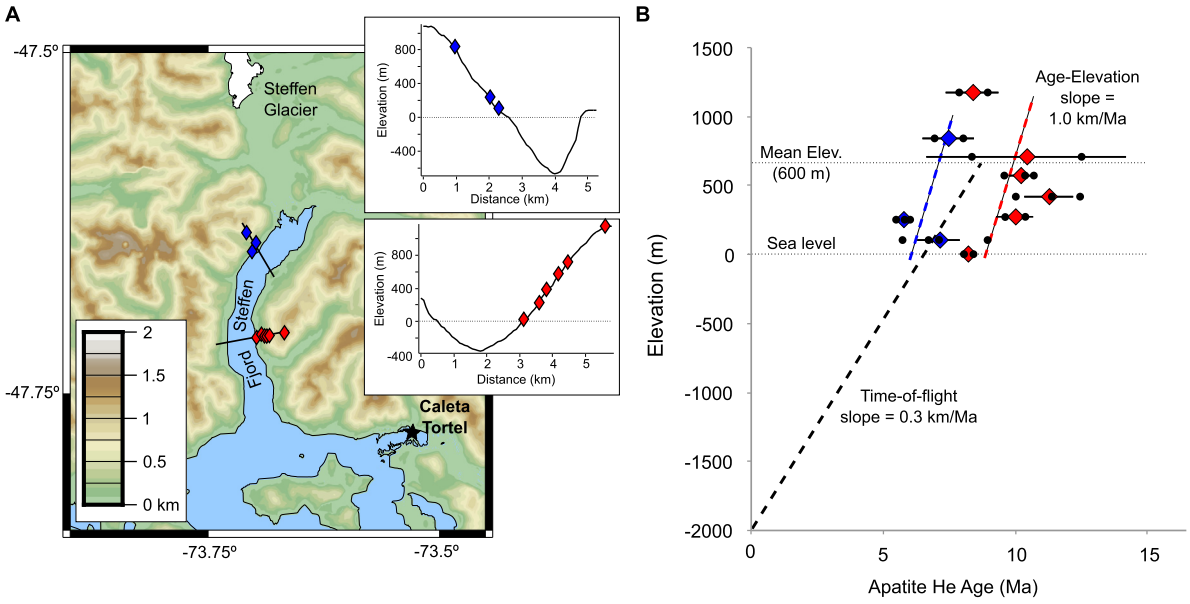

Fig. 4. Vertical transects at Fjord Steffen. (a) Topography and bedrock sample locations for vertical transects and distribution of samples in profiles across the fjord. (b) Age-elevation plot for He apatite ages. Black points are individual crystal ages, diamonds and horizontal lines are unweighted mean ages and standard error, respectively. Dashed blue lines show the local trend of the He cooling ages as a function of elevation. Dashed black line shows the time-of-flight trend as calculated using the approximate age at the mean elevation (600 m) of the local topography and the estimated depth of the closure temperature at 2 km below sea level. Together, these trends indicate fast cooling from 10 to 6 Ma and slower cooling from 8 to 0 Ma. (For interpretation of the colors in this figure, the reader is referred to the web version of this article.)

faults separating the transects in Fjord Steffen, or other evidence of young tectonic motion in the local area. Another possibility is that the offset in mean ages and ages of samples at similar elevations is due to lateral incision or headward erosion of the valley, resulting in the northern profile cooling more recently (e.g. Shuster et al., 2011).

Fig. 5 shows the observed $^4He/^3He$ ratios as a function of total ^3He abundance (black outlines) for two samples collected at sea level along the west end of Fjord Baker (see locations in Fig. 2). Six other small apatite crystals were analyzed for $^4He/^3He$ ratios. Although the data are internally consistent (Table S3), those smaller crystals did not have sufficient helium content for precise $^4He/^3He$ analyses. Therefore, our cooling history estimates are based on the remaining two samples, which did have sufficient He. The apatite He analyses of the two samples were previously reported in Thomson et al. (2010a). Sample THC07 (Fig. 5a; Table S3 THC07a) has a He age of 9.17 ± 0.22 Ma. The $^4He/^3He$ data for an individual apatite crystal from this sample indicates cooling at a rate of ~15 °C/Ma between the interval of 10 to 5 Ma (best-fit solutions shown are green paths in Fig. 5). Sample THC08 (Fig. 5b; Table S3 THC08b) has a He age of 6.43 ± 0.15 Ma and $^4He/^3He$ data that indicate a cooling rate of >30 °C/Ma at ~7 to 5 Ma. Both results indicate that the samples were at or near the surface (<35 °C) by 5 Ma.

5. Modeling cooling ages and rates

Conventional apatite He analysis provides only an age, with no direct information about temperature at that time. The usual practice is to use thermal modeling and the closure model of Dodson (1973, 1979) to calculate an effective closure temperature, which crudely provides one point on the time-temperature cooling history of an apatite crystal and its corresponding rock sample. In contrast, the $^4He/^3He$ method provides an estimate of temperature as a function of time.

We define two parameters, τ_{65} and γ_{80-35}, to summarize the cooling history as estimated by the $^4He/^3He$ method. The parameter τ_{65} indicates the time that the sample cooled through 65 °C.

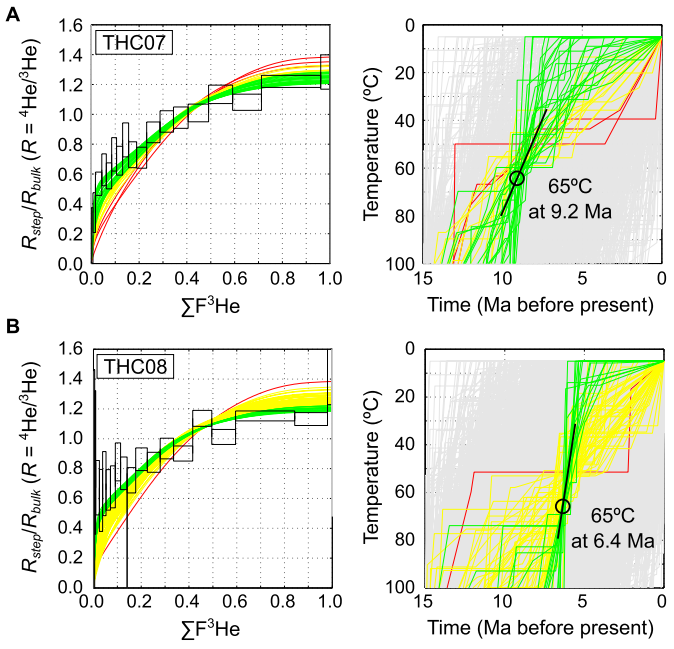

Fig. 5. $^4He/^3He$ thermochronometry and estimated cooling paths (see Fig. 2 for sample locations). In the left panels, R_{step} is the $^4He/^3He$ ratio observed at each degassing step, R_{bulk} is determined by summing all steps, and $\sum F^3He$ is the cumulative release fraction of ^3He. Open black boxes indicate 1 standard error (vertical) and integration steps (horizontal). In the right panels, the colored lines show randomly generated cooling paths that match the He age of the crystal data to within ±1 SE, and the gray lines show paths that fail to fit that data. Green paths are most consistent with the $^4He/^3He$ measurements, and yellow and red paths are progressively less consistent. (a) The $^4He/^3He$ data for THC07 indicate a mean cooling age $\tau_{65} = 9.2$ Ma and a moderate cooling rate ($\gamma_{80-35} > 15\,°C/Ma$) from 10 to 6 Ma. (b) THC08 has a mean cooling age $\tau_{65} = 6.4$ Ma and very fast cooling ($\gamma_{80-35} \sim 30\,°C/Ma$) at that time. Full degassing results are available in supplement Table S3. (For interpretation of the colors in this figure, the reader is referred to the web version of this article.)

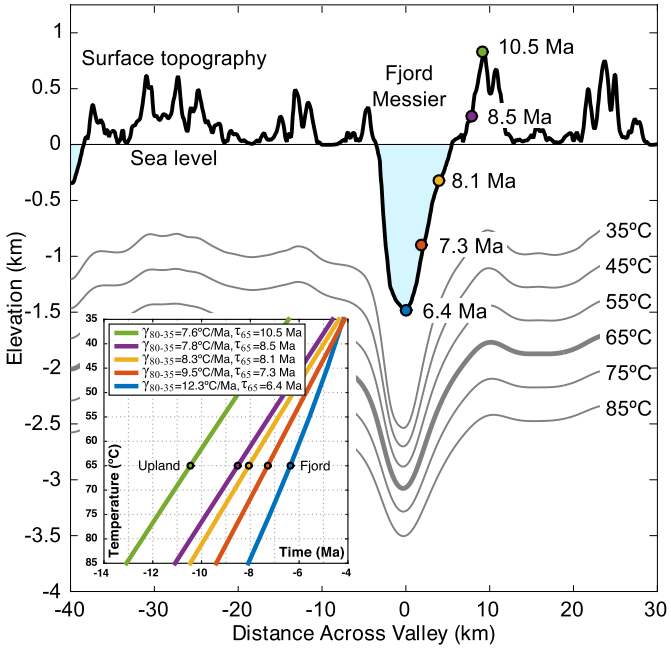

Fig. 6. Cross section of isotherm structure beneath the deepest part of Fjord Messier, assuming constant uniform erosion. The stationary topography results in a stable thermal field and therefore the isotherms are constant throughout time. For selected points in the landscape, we calculate τ_{65}, corresponding to the time since that bedrock point was at the 65 °C isotherm (colored circles), and the cooling rate, γ_{80-35} (slope of colored lines of inset plot). For this steady-state case, τ_{65} and γ_{80-35} are almost solely a function of exhumation rate. The variation in the τ_{65} ages is related to variations in the height of the locations along the fjord wall (circles) relative to the underlying 65 °C isotherm. The inset shows modeled cooling paths, where γ_{80-35} is the slope, for the locations on the fjord wall, indicating cooling rates between 8 and 12 °C/Ma at all elevations in the *Steady-state* hypothesis, shown in Fig. 7. (For interpretation of the colors in this figure, the reader is referred to the web version of this article.)

The parameter γ_{80-35} is an estimate of the average cooling rate over the interval 80 to 35 °C. The variables can be viewed as a straight-line approximation for the age-temperature path, with a point located in the center of the path, at 65 °C and age τ_{65}, and the slope of the cooling path given by γ_{80-35}. We chose the temperature 65 °C as the midpoint because it is commonly cited as the nominal closure temperature for conventional He apatite analysis, assuming a typical orogenic cooling rate of 10 °C/Ma (Shuster et al., 2006). Fig. 6 shows a simple example of modeled τ_{65} and γ_{80-35} values for a vertical suite of samples along the wall of Fjord Messier.

Much work has been done to relate thermochronometry to changes in surface topography using numerical modeling (e.g. Braun, 2003; Ehlers and Farley, 2003; Ehlers et al., 2006; Braun et al., 2012). The most common approach is to use the PECUBE program to predict the pattern of thermochronometric ages as a function of a specified history of uplift, erosion, and surface topography. Our approach differs in three ways. The first is that we use a new formulation for the evolution of surface topography. The second is that we use a Fourier-based numerical method that allows us to separate the two-dimensional evolution of the topographic surface from the more one-dimensional evolution of the thermal structure in the underlying crust as a function of a regionally average erosion rate. This methodology was first introduced in Thomson et al. (2010b). The results are equivalent to those provided by PECUBE, but the calculations are much faster, which allows for a more complete exploration of parameter space. The third difference is that we focus on how various erosion and relief scenarios influence the spatial distributions for τ_{65} and γ_{80-35}, as rendered in map view.

5.1. Topography parameterization

Topographic scenarios are constructed using a decomposed version of the modern topography. Our approach is based on the idea that tectonic uplift produces long-wavelength topography, and erosion reduces the high points of that tectonic topography and also creates incised features like valleys, due to localized erosion by rivers or glaciers. Thus, the tectonic topography can be approximated by a smoothed "draped" surface that touches only the highest summits. Consider the observed topography as represented by gridded elevations, designated by the matrix H. The matrix S represents the gridded summit topography. We estimate the summit topography using an asymmetric least-squares smoothing routine. This estimate was done using an algorithm that fits a smooth surface to an arbitrary set of 2D values (Garcia, 2010). The fit is asymmetrically weighted (Eilers and Boelens, 2005) to favor the highest points in the landscape, which gives a robust estimate of a smoothed draped surface resting on the highest summits. Given the summit topography, S, we can define a second component of the landscape, which is the valley relief, $V = S - H$.

This topography decomposition is the basis for describing candidate solutions for past topographies. We consider candidate topographies, H_c, as approximated by a scaled linear combination of the summit and valley components of the modern topography, as indicated by $H_c = f_v V + f_s S$. The two parameters, f_v and f_s, provide a simple representation of a wide range of plausible topographies. For example, $f_v = f_s = 1$ represents the modern topography. Braun (2003) uses a similar approach for his PECUBE program. There the candidate topographies are defined by $H_c = f_a H + f_o$,

where the parameters, f_a and f_o, are amplification and offset factors, respectively.

5.2. Predicted closure surface

We use a two-component thermal model for estimating the depth and thermal gradient associated with the 35, 65, 80 °C isotherms. The first component is a one-dimensional regional thermal field defined by an infinite layer with horizontal upper and lower surfaces. The upper surface is fixed at the mean elevation and the lower surface at 30 km below the mean elevation. The second component represents the influence of topography on the underlying thermal field in three dimensions, which is calculated using a third-order Fourier-series solution (Fyrillas and Pozrikidis, 2001). We use thermal parameters specific to our study region, including a thermal diffusivity of 32 km^2/Ma (∼1 mm^2/s), and a regional erosion rate of 0.25 km/Ma (Thomson et al., 2010a; Herman and Brandon, 2015). The internal heat production has little effect for this problem, and is thus set to zero. The temperature at the mean elevation is set to 0 °C, which is consistent with the expected long-term temperature of the atmosphere at that elevation. The temperature at the base of the model is set to 750 °C, which gives an average geothermal gradient of ∼25 °C/km and a surface heat flow consistent with modern measurements (Hamza et al., 2005). The surface topography is overlain by air above sea level and water below sea level. The surface boundary is dominated by the submarine part of the topography. The water column has little to no thermal gradient, so we set the surface lapse rate of the model to 0 °C/km.

The examples used here are focused on the influence of changes in topography on τ_{65} and γ_{80-35}, and by extension, observed apatite He ages and $^4He/^3He$ data. For this purpose, the regional erosion rate is held at constant value, which means that the one-dimensional regional thermal structure remains steady. The shallow thermal structure adjusts quickly to changes in valley topography (∼0.1 Ma response time) given the shallow depth of the 35 to 80 °C isotherms relative to the surface boundary (Stüwe and Hintermüller, 2000). As a result, the time lag between valley incision and the response of the 35 to 80 °C isotherms can be ignored. Thus, we can assume a quasi-steady relationship between the surface boundary condition and the shallow isotherms.

Our approach allows for a decoupled analysis of the evolution of summit topography and valley relief, as applied to morphological evolution of the topography and also to the evolution of the shallow thermal field beneath the topography. The summit topography is mainly created by tectonic processes operating at the regional scale, whereas the valley topography is mainly created by incision by rivers and glaciers. Thus, our topographic parameterization emphasizes the evolution of summit topography, as controlled by tectonic uplift and an average erosion rate at a regional scale, and by valley incision, which can be viewed as variations in erosion at a local scale. The thermal modeling is likewise decoupled in a similar way. The 1D component of the thermal model represents the thermal evolution at a regional scale as a function of the regional erosion rate, which is recorded by our cooling ages as a regional exhumation rate. The topographic component of the thermal model accounts for the evolution of the thermal field as a function of changing valley relief. These two components can be calculated separately, which allows for an easier understanding about how regional erosion and valley relief influence cooling ages.

5.3. Map view prediction of cooling ages and rates

Bedrock cooling ages are simply the intersection of isochrones with modern topography. To calculate τ_{65} values for the modern bedrock surface, we approximate the 3-dimensional shape of the 65 °C isotherm through time (as prescribed by a topographic scenario outlined in section 6.1) and advect it vertically at the regional exhumation rate (0.25 km/Ma). For example, the 6 Ma isochrone represents the shape of the 65 °C isotherm at 6 Ma. Given the regional exhumation rate, this isochrone should currently be at a vertical height of 1.5 km above the modern 65 °C isotherm.

To model average cooling rates between 80 and 35 °C, γ_{80-35}, the 3-dimensional shape of the 80 and 35 °C isotherms through time are advected at the regional exhumation rate. Therefore, each point at the surface has two additional "cooling ages", τ_{80} and τ_{35} that indicate the time since passing through the 80, and 35 °C isotherms, respectively. The cooling rate is equivalent to the difference in temperature, divided by the difference in age: $(80–35\,°C)/(\tau_{80}-\tau_{35})$.

6. Thermochronometric signals for topographic evolution

6.1. Modeled valley incision scenarios

We consider several hypotheses that illustrate how thermochronometric results vary as a function of different topographic scenarios (Fig. 7). Each of the hypotheses described below was chosen to highlight the connection between specific thermochronometric outcomes and a broader topical issue.

Steady-state: For this reference hypothesis, topography maintains a constant form with time, which requires the exhumation rate to be spatially uniform. In practical terms, this scenario describes an "antecedent landscape", which means that the shape of the topography was formed prior to the onset of glaciation. This possibility is unlikely in Patagonia, given the fact that the modern landscape is laced with kilometer-deep fjords, but it provides a useful reference for the following alternative hypotheses.

Early Incision: Valley relief is created rapidly after the onset of mountain glaciation. This scenario is motivated by the presence of glacial till dating to ∼7 to 5 Ma (Mercer and Sutter, 1982; Ton-That et al., 1999) and follows the widely held view that glaciers are more erosive than rivers (see discussions in Hallet et al., 1996; Brocklehurst and Whipple, 2006; Koppes and Montgomery, 2009; Yanites and Ehlers, 2012).

Steady Incision: Valley relief is formed at an approximately steady rate. This scenario is based on the idea of a negative feedback between glacial erosion and topography (Oerlemans, 1984; MacGregor et al., 2000; Kaplan et al., 2009; Shuster et al., 2011). Glacial erosion tends to reduce the ice catchment (accumulation zone) required to feed the glacier. As a result, the rate of glacial erosion is linked to the long-term evolution of the ELA. Late Cenozoic cooling has caused a long-term lowering of the ELA in temperate latitudes. The idea is that valley incision would proceed at a similar rate.

Late Incision: Valley relief formed recently (<∼2 Ma). This scenario is motivated by two previous $^4He/^3He$ apatite studies in mountain landscapes elsewhere that show an onset of rapid glacial incision at ∼1 Ma (Shuster et al., 2011; Valla et al., 2011). Timing might be related to the mid-Pleistocene transition (1.2 to 0.7 Ma), when glacial–interglacial cycle changed from a period of 41 ka to 100 ka (e.g. Pedersen and Egholm, 2013). A similar timing in southern Chile would be interesting, given that glaciations there started much earlier, by at least ∼7 to 5 Ma, than in most other alpine glaciated settings (e.g. 2.6 Ma in the European Alps; Preusser, 2012).

6.2. Cooling age and rate model results

The results of the model are summarized in Fig. 7. Column 1 provides an expanded view of the predictions for the *Steady-state*

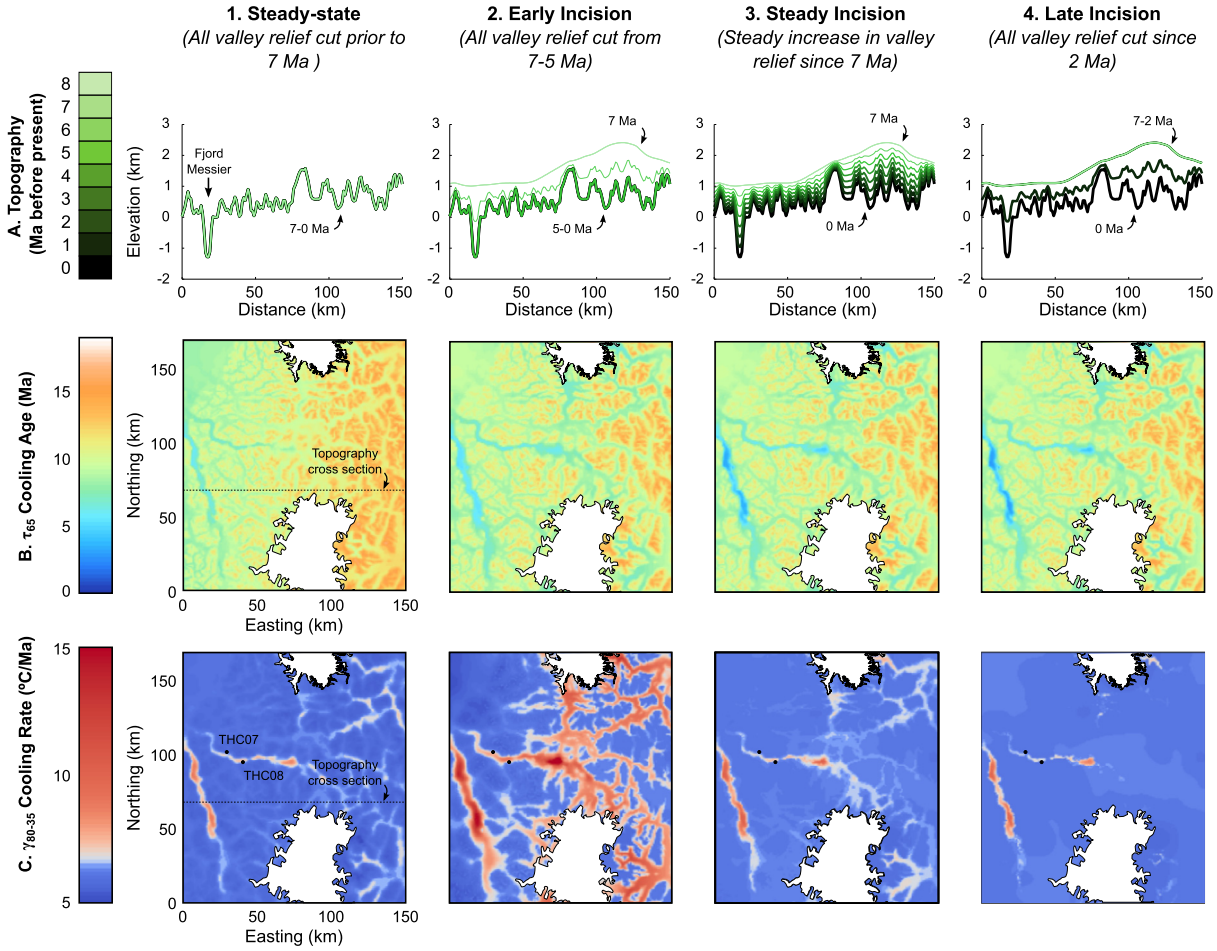

Fig. 7. Model simulation for four topographic scenarios. The *Steady-State* (null) hypothesis is shown in the left column, and the remaining columns show three alternative hypotheses (see text for details). The top row shows cross sections through the modeled topography across Fjord Messier for the four topographic scenarios at 1 Ma intervals from 7 Ma (thick light green line) to the modern (thin black line). The *Steady-state* scenario (column 1) has a steady topographic form, equivalent to the modern topography. The three alternative hypotheses (columns 2–4) start with a relatively smooth topography, with initial elevations similar to the modern summit topography. For each scenario, the valley relief is then increased at different times until it develops to the modern topography. The second and third rows show predictions for τ_{65} (cooling age since 65 °C) and γ_{80-35} (cooling rates for the interval 80 to 35 °C) for each scenario as observed in bedrock samples from the modern topographic surface. (For interpretation of the colors in this figure, the reader is referred to the web version of this article.)

case relative to Fig. 6. Bedrock in the summit regions are distinguished by old cooling ages (∼15 Ma) and low cooling rates (∼5 °C/Ma). Valleys have intermediate ages (8 to 10 Ma) and low cooling rates (∼7 °C/Ma). The deeply incised fjords have young ages (∼6 Ma) and moderate cooling rates (∼8 to 12 °C/Ma). The predicted cooling ages are primarily a function of elevation above the closure surface. Predicted ages are younger at low elevation and older at high elevations. Note that all of the scenarios predict faster cooling beneath fjords relative to summits because near-surface isotherms are always compressed beneath the valleys and expanded beneath summits (e.g., Fig. 6).

The alternative hypotheses (Fig. 7, Columns 2–4) highlight the ability of low-temperature thermochronometric data to resolve the timing and rates associated with changes in relief. These models each predict identical He ages and cooling rates (τ_{65} and γ_{80-35}) in summit regions because the forward models are initiated with the same steady-state, low-relief topography from 15 to 7 Ma. The thermochronometric predictions for the alternative hypotheses begin to diverge at 7 Ma. This difference is recorded in modern bedrock exposures at ∼0 m elevation and varies based on the local depth to the 65 °C isotherm. The largest difference in cooling ages between the modeled scenarios is at the lowest elevations in the landscape, which is the bottom of the fjords. Our observations are limited to where we can sample, at elevations between 0 to 1200 m (Fig. 2). The calculations show that while there are slight differences in predicted He ages for end-member topographic scenarios at 0 to 1200 m, these differences are within the uncertainty for the ages, which is typically ∼10% (Farley, 2002). Thus, He ages from subaerial outcrops are unable to distinguishing between the competing topographic scenarios.

^{4}He/^{3}He thermochronometry provides a way forward. In the *Early Incision* scenario (Fig. 7, Column 2), the model predicts relatively rapid cooling (high cooling rates) in the valleys and fjords. The *Early Incision* scenario illustrates fast erosion of the valleys from 7 to 5 Ma, which results in fast cooling there from 7 to 5 Ma. The *Steady Incision* scenario (Fig. 7, Column 3) illustrates the prediction for a landscape in which the valley depth increases gradually over time. In this scenario, erosion of the valleys and fjords proceeds at a greater rate than erosion in the upland regions. As a result, the fjords show faster cooling relative to the upland areas over the last 7 Ma. The *Late Incision* scenario postulates that the valley relief formed during the last 2 Ma. In this scenario, the model predicts that the fjords would be floored by young cooling ages of ∼1–2 Ma with high cooling rates. In contrast, the upper parts of the valley (presently above sea level) and the upland areas would have cooling ages older than ∼6 Ma and lower cooling rates.

7. Discussion

7.1. Comparison of model results and data

The map-based predictions of cooling ages and rates allow us to directly compare the spatial pattern of the He ages and ^{4}He/^{3}He data resulting from different topographic scenarios (Fig. 7). Here we compare the four models to the key constraints in our data: The He ages from the Fjord Steffen transects (Table 1) and the exhumation rate estimates derived from the age-elevation plot (Fig. 4), and the cooling history information from the sea level samples along Fjord Baker (Fig. 5).

The observed He ages, which range from 5.8 to 11.3 Ma (Table 1), do not constrain the topographic history because the scenarios predict similar modeled He ages within the available sampling range, between 0 to 1200 m elevation. The time-of-flight exhumation rate of ∼0.3 km/Ma fails to resolve any change in exhumation rate associated with glacial erosion that might have happened since ∼8 Ma because the time-of-flight exhumation rate is averaged over the interval of 8 Ma to the present.

The individual cooling histories of the two samples from Fjord Baker (Fig. 5) are needed to resolve changes in exhumation rate since 8 Ma. Both ^{4}He/^{3}He release spectra indicate that the samples cooled rapidly from high temperatures (>85 °C), through the closure temperature and below 35 °C between 10 and 5 Ma. The *Early Incision* landscape evolution model (Column 2 in Fig. 7), where incision occurred rapidly between 7 to 5 Ma, is the only scenario in which samples currently at subaerial locations have estimated fast cooling rates. We therefore conclude that the results of early rapid cooling at a rate of 15–30 °C/Ma between 10 to 5 Ma show that early glaciations in central Patagonia rapidly eroded valleys into the landscape, and the modern observed valley relief was formed by ∼5 Ma.

Others have proposed tectonic and geodynamic interpretations for evolution of topography in this region (e.g., Cande and Leslie, 1986; Ramos and Ghiglione, 2008; Guillaume et al., 2013; Braun et al., 2013; Georgieva et al., 2016). He age data from this study reveal a fast exhumation rate between ∼0.5 to 1 km/Ma from 10 to 6 Ma. Guillaume et al. (2013) report a similar trend in He age with elevation in both the Cerros Barrancos region, ∼75 km east of Fjord Steffen, and farther northeast along the margin of Lago General Carrera. They find apatite He ages between 5 and 10 Ma that indicate exhumation rates of ∼0.5 km/Ma over this duration. Georgieva et al. (2016) find a similar trend in He ages in vertical transects in glacial valleys east of the NPI. Farther afield, a study in the southern Andes (∼51°S), finds young apatite He ages (<10 Ma) that are interpreted as a record of glacial erosion starting at ∼7 Ma (Fosdick et al., 2013). Importantly, we show that these thermochronometric datasets can be explained entirely by rapid increase in valley relief between ∼10 to 5 Ma. This is in contrast to the interpretation of Guillaume et al. (2013), which attributes the observed cooling to dynamic topography associated with the slab window.

The topography around the Patagonian fjords between 47.5 and 48.5°S has both a lower mean elevation and lower summit elevations than the topography to the north and south (the regions currently covered by the NPI and SPI). Georgieva et al. (2016) attribute the anomalously low elevation of this region to margin-parallel extension related to the subduction of ridge segments at the Chile triple junction since 2–3 Ma. Lowering the mean topographic elevation in this region could occur by block subsidence, erosion of the surface, or a combination of the two. While our data are technically consistent with block subsidence since 2–3 Ma, there is no independent evidence for a block subsidence scenario. Our thermochronometric data do preclude large-scale erosion of the topography since 5 Ma. Erosion of the surface causes rocks to be exhumed towards the Earth's surface. Because the upper crustal thermal field is coupled to the surface boundary condition, a large-scale erosional event lowering the topographic surface would be captured in the low-temperature thermochronometric data. The ^{4}He/^{3}He cooling histories from this area show that the bedrock cooled to surface temperatures by 5 Ma, indicating very slow exhumation and therefore minor erosion of the topography since 5 Ma.

Given that the thermochronometric data can be explained entirely by a regional exhumation rate of 0.25 km/Ma with an increase in valley relief at ∼7 Ma, along with the lack of structural evidence for modification by tectonics in the fjords, and the results of modeling the upper crustal temperature above the ridge subduction (Fig. 3) which shows a negligible effect of Chile triple junction on the upper crustal thermal field, we prefer a glacial erosion model for the central Patagonian Andes. The primary topographic change in our study area was the punctuated incision of valleys and fjords soon after the onset of glaciation. Early glaciations caused rapid erosion of the fjords in our study area until ∼5 Ma, when samples that are currently at sea level exhumed to temperatures less than ∼35 °C. Neotectonic activity, recognized by Georgieva et al. (2016) on the eastern flank of the NPI, and thought to be active since ∼2–3 Ma, are not resolved by our thermochronometric data or in our thermal–kinetic model. However, our data do require slow erosion and therefore little topographic change in the fjords since ∼5 Ma.

7.2. Thermochronometric signatures of the timing of valley incision

The thermal–kinetic model gives a map view of the thermochronometric signature of valley relief formation scenarios (Fig. 7). While the model results presented in this paper are specific to Patagonia, the method provides insight into the valley incision problem in general and the resolution of low-temperature thermochronometric data. The modeled cooling information shows how the spatial patterns of He ages and cooling rates (τ_{65} and γ_{80-35}) constrain landscape evolution. Specifically, Fig. 7 shows that ^{4}He/^{3}He is needed to resolve valley incision and that there are predictable patterns of thermochronometric cooling data for given landscape evolution scenarios.

To further illustrate this concept, consider another example from the upper Rhône Valley in the Swiss Alps (Fig. 8; Valla et al., 2011). Apatite He ages from an elevation traverse in the upper Rhône Valley increase monotonically from 4 to 8 Ma, with increasing elevation (Fig. 8b). The elevation-age gradient, ∼0.6 km/Ma, estimates the exhumation rate from 8 to 4 Ma and the He age at the current mean elevation indicates an average exhumation rate of ∼0.3 km/Ma over the interval from 6 to 0 Ma. As with our He age results from Patagonia, the He ages alone fail to resolve any change in exhumation rate associated with glacial erosion, which started at 2.6 Ma in the Alps (Preusser, 2012). ^{4}He/^{3}He thermochronometry is needed to adequately resolve the exhumation history during this younger interval. In the Alps, a valley-bottom sample (Fig. 8e, SIO-04) experienced fast cooling starting at ∼1 Ma, while a high-elevation sample (Fig. 8c, SIO-06) was near the Earth's surface by ∼2.5 Ma, indicating that the cooling was related to an increase of valley relief of ∼1 km (i.e., the difference in elevation of the samples).

The Rhone Valley data provide a characteristic example of a young valley incision event, where formation of the valley relief postdates the bedrock apatite He ages observed at the surface. In contrast, the observed He data in Patagonia, as illustrated in *Early Incision* landscape evolution model (Row 2 in Fig. 7), show a characteristic example in which the formation of valley relief coincides with the timing of the closure of the He system. A third end-member scenario, illustrated by the *Steady incision* case in Fig. 7

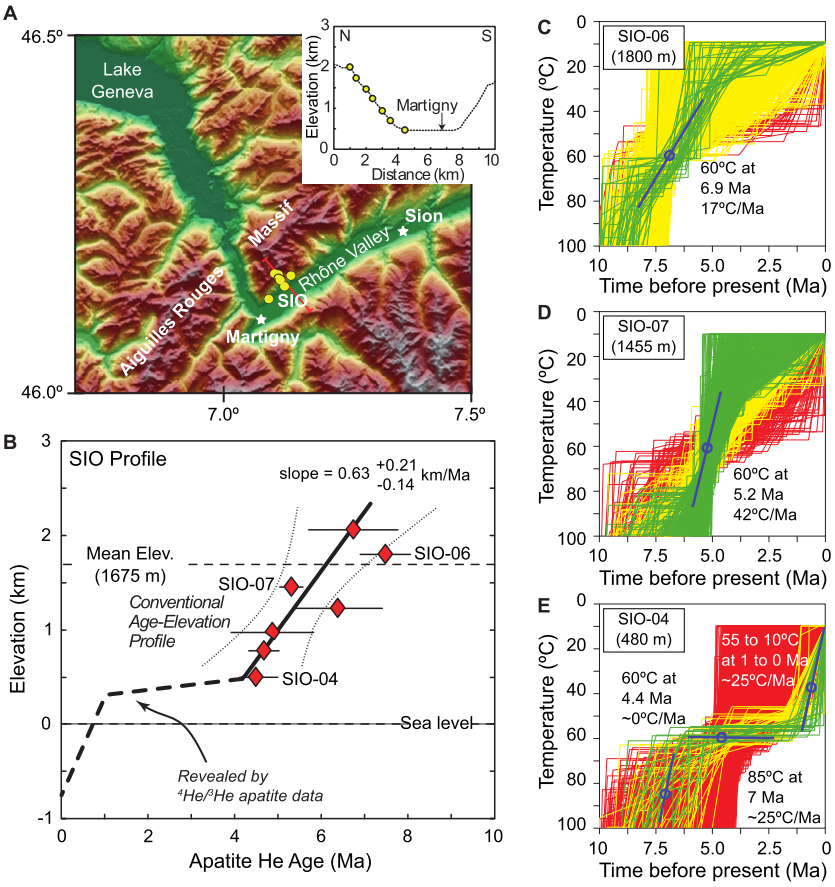

Fig. 8. An example from the Rhône Valley in the Swiss Alps showing how apatite He ages and $^4He/^3He$ data constrain long-term erosion and valley incision (modified after Valla et al., 2011). (a) Vertical transect sample locations (yellow circles). (b) Apatite He ages increase from ~4 to 8 Ma with elevation. Error bars are equal to ±1 SE. Envelope and errors for the regression line are shown at the 95 percent confidence level. Dashed line shows an approximate extrapolation of the age-elevation profile, as guided by the $^4He/^3He$ results. The extrapolation shows that the conventional He apatite ages could be used to resolve the young event, but that would require analysis of bedrock samples from below the valley floor. (c–e) Cooling paths constrained by $^4He/^3He$ data for three samples, shown in order, from top to bottom, of decreasing elevation. The colored lines show randomly generated cooling paths that match the He age to within ±1 SE, and the gray lines show paths that fail to fit those data. Green paths are most consistent with the $^4He/^3He$ measurements, and yellow and red paths progressively less consistent. See text for interpretation. (For interpretation of the colors in this figure, the reader is referred to the web version of this article.)

Row A, shows the thermochronometric signature of an old incision event, where the formation of valley topography pre-dates the closure of the samples currently at the surface. In each case, the thermochronometric signature is distinct timing of cooling in bedrock at different vertical positions and only a small number of samples are needed to resolve the timing of valley formation.

Finally, our results also highlight the importance of the regional exhumation rate in controlling the thermochronometric record. A common strategy in thermochronometric studies is to sample over a large vertical range to ensure a long record of cooling ages. However, the duration of that record is a function of both the vertical sampling range and the regional exhumation rate. The regional exhumation rate in central Patagonia is relatively low, ~0.25 km/Ma, which means that there is a large range of cooling ages in the vertical. This feature is like a condensed stratigraphic section, which is characterized by a long time range in a short section. $^4He/^3He$ thermochronometry is especially useful in this setting in that we are provided with a long record of very-low temperature cooling. To illustrate, consider the *Steady* and *Late Incision* scenarios, where fast cooling would only be observed in bedrock surfaces currently below sea level. In contrast, consider the thermochronometric record of glacial incision in Fiordland, New Zealand, where the regional exhumation rate is four times faster (Shuster et al., 2011). This scenario, which is not illustrated in Fig. 7, would have very young cooling ages in all areas including the highest summits. For Fiordland, the subaerial topography, which reaches ~1.5 km above sea level, has only a short range of cooling ages, spanning ~1 to 2 Ma. This case is analogous to an expanded stratigraphic section, where the age range is unexpectedly small. The important point is the apatite He ages cannot provide any information about the formation of that landscape prior to 2 Ma. However, the subaerial bedrock in that area preserves an excellent record of the young evolution of that glacial landscape (Shuster et al., 2011).

7.3. Implications for understanding of glacial erosion

Much of the debate about long-term results of glacial erosion has focused on how glaciers have resculpted the tops of mountains, by lowering summits or enlarging cirques (Porter, 1989; Brocklehurst and Whipple, 2006; Oskin and Burbank, 2005; Egholm et al., 2009). Our work here focuses on the lowest parts of the glacial landscape, which are ubiquitous in continental regions at high latitudes around the globe. We find evidence for two interesting conclusions: 1) that valley incision has dominated much of the topographic evolution of the central Patagonian Andes, and 2) that the cutting of those valleys occurred shortly after the start of alpine glaciations. What is surprising is how slow erosion has been since 5 Ma. To emphasize this point, consider that our sea level samples have been at temperatures less than 35 °C since 5 Ma, indicating erosion rates of <0.2 km/Ma. This conclusion is perhaps expected given our current understanding of glacial

erosion. The first is the negative feedback between glaciation and erosion. As glaciation progresses, the elevation of the upstream accumulation zone is gradually eroded (Oerlemans, 1984; Anderson et al., 2012). In other words, glaciers tend to cannibalize their ice catchment, leading to a progressive decrease in ice discharge and erosion at some time after the start of alpine glaciations. A second related effect is that the lowering of bedrock by erosion results in thicker ice during subsequent glaciations. Thicker ice should have lower basal sliding velocities, assuming that the ice discharge remains the same. A third effect is that Late Cenozoic cooling leads to an increase of cold-based ice. All of these factors would lead to a reduction in glacial erosion rates with time.

Our results also have implications for our understanding of the feedbacks between global climate and timing of glacial erosion. The Central Patagonian Andes have a record of early alpine glaciations, and our work now demonstrates an early history of valley incision, both prior to ∼5 Ma. These results are in stark contrast to other mid-latitude settings, especially in the northern hemisphere, where alpine glaciations started in the early Pleistocene (e.g., 2.6 Ma in the Alps; Preusser, 2012). There has been much discussion about the possibility that the mid-Pleistocene glacial transition (1.2 to 0.7 Ma; Berger et al., 2008) may have marked a time of increased glacial incision around the world (Valla et al., 2011; Herman et al., 2013; Pedersen and Egholm, 2013). Based on our work, we see an equally viable interpretation that rapid valley incision is associated with the onset of alpine glaciations. This alternative explanation explains the observed fast incision in Patagonia soon after the first known glaciations and other mid-latitude settings where the timing of the onset of glaciation is known. We leave open the possibility that global climate change influences glacial erosion rates in Patagonia and elsewhere. The results presented in this paper do not resolve erosional events younger than ∼5 Ma. Patagonia is an interesting location to explore the influence of the mid-Pleistocene glacial transition, especially given the depth of the fjords, which we show in our model may contain a thermochronometric record of young erosional events in bedrock beneath sea level.

8. Conclusions

In this study, we illustrate how low-temperature thermochronometry can constrain the timing of glacial valley incision in Patagonia. Our thermal–kinetic modeling results show the resolution of apatite He data and the distinct thermochronometric signatures for different topographic scenarios. Apatite He ages and ^{4}He/^{3}He thermochronometry from southern Chile require rapid cooling between 10 to 5 Ma. We show that migration of the Chile triple junction had a negligible influence on the thermal structure of the shallow crust in the Patagonian forearc. Therefore, we conclude the thermochronometric signal of fast cooling is likely due to an increase in valley relief coinciding with early glaciations in the Andes. Erosion rates in the trunk valleys far outpaced erosion in the summits or hanging valleys and valley incision proceeded rapidly. Samples currently at sea level were near the surface by ∼5 Ma. These results suggest that the primary topographic effect of glacial erosion is the incision of valleys and fjords soon after the onset of glaciation.

Acknowledgements

We would like to thank Stuart Thomson for providing samples for apatite ^{4}He/^{3}He analysis, Wendy DeWolf and Ryan Laemel for their help collecting and processing samples, and Nick Fylstra for laboratory assistance. Fieldwork was only possible given the logistical support provided by Noel Vidal and Maria Paz Hargreaves (Entre Hielos, Caleta Tortel). We would also like to thank Keith Ma for many discussions about the glacial history of Patagonia that inspired this work. Eva Enkelmann and an anonymous reviewer provided thoughtful comments that improved the manuscript. Christeleit acknowledges support from a NSF Graduate Research Fellowship, Yale University, and the Yale Institute for Biospheric Studies. Shuster acknowledges the support of the Ann and Gordon Getty Foundation.

Appendix A. Supplementary material

Supplementary material related to this article can be found online at http://dx.doi.org/10.1016/j.epsl.2016.12.019.

References

Alley, R.B., Lawson, D.E., Larson, G.J., Evenson, E.B., Baker, G.S., 2003. Stabilizing feedbacks in glacier-bed erosion. Nature 424, 758–760.
Anderson, R.S., Dühnforth, M., Colgan, W., Anderson, L., 2012. Far-flung moraines: exploring the feedback of glacial erosion on the evolution of glacier length. Geomorphology 179, 269–285.
Araya-Vergara, J.F., 2008. The submarine geomorphology of the Chilean Patagonian fjords and piedmonts. In: Silva, N., Palma, S. (Eds.), Progress in the Oceanographic Knowledge of Chilean Interior Waters, from Puerto Montt to Cape Horn, pp. 25–27.
Berger, A.L., Gulick, S.P., Spotila, J.A., Upton, P., Jaeger, J.M., Chapman, J.B., Worthington, L.A., Pavlis, T.L., Ridgway, K.D., Willems, B.A., McAleer, R.J., 2008. Quaternary tectonic response to intensified glacial erosion in an orogenic wedge. Nat. Geosci. 1, 793–799.
Blisniuk, P.M., Stern, L.A., Chamberlain, C.P., Idleman, B., Zeitler, P.K., 2005. Climatic and ecologic changes during Miocene surface uplift in the Southern Patagonian Andes. Earth Planet. Sci. Lett. 230, 125–142.
Braun, J., 2003. Pecube: a new finite-element code to solve the 3D heat transport equation including the effects of a time-varying, finite amplitude surface topography. Comput. Geosci. 29, 787–794.
Braun, J., van Der Beek, P., Valla, P., Robert, X., Herman, F., Glotzbach, C., Pedersen, V., Perry, C., Simon-Labric, T., Prigent, C., 2012. Quantifying rates of landscape evolution and tectonic processes by thermochronology and numerical modeling of crustal heat transport using PECUBE. Tectonophysics 524, 1–28.
Braun, J., Robert, X., Simon-Labric, T., 2013. Eroding dynamic topography. Geophys. Res. Lett. 40, 1494–1499.
Breitsprecher, K., Thorkelson, D.J., 2009. Neogene kinematic history of Nazca–Antarctic–Phoenix slab windows beneath Patagonia and the Antarctic Peninsula. Tectonophysics 464, 10–20.
Brocklehurst, S.H., Whipple, K.X., 2006. Assessing the relative efficiency of fluvial and glacial erosion through simulation of fluvial landscapes. Geomorphology 75, 283–299.
Caldenius, C.G., 1932. Las glaciaciones Cuaternarias en la Patagonia y Tierra del Fuego. Dirección General de Minas y Geología.
Cande, S.C., Leslie, R.B., 1986. Late Cenozoic tectonics of the Southern Chile Trench. J. Geophys. Res. 91, 471–496.
Clapperton, C.M., 1993. Quaternary Geology and Geomorphology of South America. Elsevier, New York. 779 pp.
Dodson, M.H., 1973. Closure temperature in cooling geochronological and petrological systems. Contrib. Mineral. Petrol. 40, 259–274.
Dodson, M.H., 1979. Theory of cooling ages. In: Lectures in Isotope Geology. Springer, Berlin, Heidelberg, pp. 194–202.
Dowdeswell, J.A., Vásquez, M., 2013. Submarine landforms in the fjords of southern Chile: implications for glacimarine processes and sedimentation in a mild glacier-influenced environment. Quat. Sci. Rev. 64, 1–19.
Egholm, D.L., Nielsen, S.B., Pedersen, V.K., Lesemann, J.E., 2009. Glacial effects limiting mountain height. Nature 460, 884–887.
Ehlers, T.A., Farley, K.A., 2003. Apatite (U–Th)/He thermochronometry: methods and applications to problems in tectonic and surface processes. Earth Planet. Sci. Lett. 206, 1–14.
Ehlers, T.A., Farley, K.A., Rusmore, M.E., Woodsworth, G.J., 2006. Apatite (U–Th)/He signal of large-magnitude accelerated glacial erosion, southwest British Columbia. Geology 34, 765–768.
Eilers, P., Boelens, H., 2005. Baseline correction with asymmetric least squares smoothing. Leiden University Medical Centre report.
Farley, K.A., 2002. (U–Th)/He dating: techniques, calibrations, and applications. Rev. Mineral. Geochem. 47, 819–844.
Flowers, R.M., Farley, K.A., 2012. Apatite ^{4}He/^{3}He and (U–Th)/He evidence for an ancient Grand Canyon. Science 338, 1616–1619.
Fosdick, J.C., Grove, M., Hourigan, J.K., Calderon, M., 2013. Retroarc deformation and exhumation near the end of the Andes, southern Patagonia. Earth Planet. Sci. Lett. 361, 504–517.

Fyrillas, M., Pozrikidis, C., 2001. Conductive heat transport across rough surfaces and interfaces between two conforming media. Int. J. Heat Mass Transf. 44, 1789–1801.
Garcia, D., 2010. Robust smoothing of gridded data in one and higher dimensions with missing values. Comput. Stat. Data Anal. 54, 1167–1178.
Georgieva, V., Melnick, D., Schildgen, T.F., Ehlers, T.A., Lagabrielle, Y., Enkelmann, E., Strecker, M.R., 2016. Tectonic control on rock uplift, exhumation, and topography above an oceanic ridge collision: Southern Patagonian Andes (47°S), Chile. Tectonics 35, 1317–1341.
Glasser, N.F., Ghiglione, M.C., 2009. Structural, tectonic and glaciological controls on the evolution of fjord landscapes. Geomorphology 105, 291–302.
Guillaume, B., Gautheron, C., Simon-Labric, T., Martinod, J., Roddaz, M., Douville, E., 2013. Earth Planet. Sci. Lett. 364, 157–167.
Guivel, C., Morata, D., Pelleter, E., Espinoza, F., Maury, R.C., Lagabrielle, Y., Polvé, M., Bellon, H., Cotten, J., Benoit, M., Suárez, M., 2006. Miocene to Late Quaternary Patagonian basalts (46–47°S): geochronometric and geochemical evidence for slab tearing due to active spreading ridge subduction. J. Volcanol. Geotherm. Res. 149, 346–370.
Hallet, B., Hunter, L., Bogen, J., 1996. Rates of erosion and sediment evacuation by glaciers: a review of field data and their implications. Glob. Planet. Change 12, 213–235.
Hamza, V.M., Dias, F.J.S.S., Gomes, A.J.L., Terceros, Z.G.D., 2005. Numerical and functional representations of regional heat flow in South America. Phys. Earth Planet. Inter. 152, 223–256.
Haschke, M., Sobel, E.R., Blisniuk, P., Strecker, M.R., Warkus, F., 2006. Continental response to active ridge subduction. Geophys. Res. Lett. 33, L15315.
Headley, R.M., Roe, G., Hallet, B., 2012. Glacier longitudinal profiles in regions of active uplift. Earth Planet. Sci. Lett. 317, 354–362.
Herman, F., Seward, D., Valla, P.G., Carter, A., Kohn, B., Willett, S.D., Ehlers, T.A., 2013. Worldwide acceleration of mountain erosion under a cooling climate. Nature 504, 423–426.
Herman, F., Brandon, M.T., 2015. Mid-latitude glacial erosion hotspot due to equatorial shifts in southern Westerlies. Geology 43, 987–990.
Hooke, R.L., 1991. Positive feedbacks associated with erosion of glacial cirques and overdeepenings. Geol. Soc. Am. Bull. 103, 1104–1108.
Hulton, N., Sugden, D., Payne, A., Clapperton, C., 1994. Glacier modeling and the climate of Patagonia during the last glacial maximum. Quat. Res. 42, 1–19.
Kaplan, M., Hein, A., Hubbard, A., Lax, S., 2009. Can glacial erosion limit the extent of glaciation? Geomorphology 103, 172–179.
Kessler, M.A., Anderson, R.S., Briner, J.P., 2008. Fjord insertion into continental margins driven by topographic steering of ice. Nat. Geosci. 1, 365–369.
Koppes, M.N., Montgomery, D.R., 2009. The relative efficacy of fluvial and glacial erosion over modern to orogenic timescales. Nat. Geosci. 2, 644–647.
MacGregor, K.R., Anderson, R.S., Anderson, S.P., Waddington, E.D., 2000. Numerical simulations of glacial-valley longitudinal profile evolution. Geology 28, 1031–1034.
McPhillips, D., Brandon, M.T., 2010. Using tracer thermochronology to measure modern relief change in the Sierra Nevada, California. Earth Planet. Sci. Lett. 296, 373–383.
Mercer, J.H., Sutter, J.F., 1982. Latest Miocene–earliest Pliocene glaciation in Southern Argentina: implications for global ice sheet history. Palaeogeogr. Palaeoclimatol. Palaeoecol. 38, 185–206.
Molnar, P., England, P., 1995. Temperatures in zones of steady-state underthrusting of young oceanic lithosphere. Earth Planet. Sci. Lett. 131, 57–70.
Montgomery, D.R., 2002. Valley formation by fluvial and glacial erosion. Geology 30, 1047–1050.
Oerlemans, J., 1984. Numerical experiments on large-scale glacial erosion. Z. Gletsch.kd. Glazialgeol. 20, 107–126.
Oskin, M., Burbank, D.W., 2005. Alpine landscape evolution dominated by cirque retreat. Geology 33, 933–936.
Pedersen, V.K., Egholm, D.L., 2013. Glaciations in response to climate variations preconditioned by evolving topography. Nature 493, 206–210.
Porter, S.C., 1989. Some geological implications of average Quaternary glacial conditions. Quat. Res. 32, 245–261.
Preusser, F., 2012. Quaternary glaciation history of northern Switzerland. Quat. Int. 279–280, 386.
Ramos, V.A., 1989. Andean foothills structures in Northern Magallanes Basin, Argentina. Am. Assoc. Pet. Geol. Bull. 73, 887–903.
Ramos, V., Ghiglione, M., 2008. Tectonic evolution of the Patagonian Andes. Dev. Quat. Sci. 11, 57–71.
Ramsay, A.C., 1862. On the glacial origin of certain lakes in Switzerland, the black forest, Great Britain, Sweden, North America, and elsewhere. J. Geol. Soc. 18, 185–205.
Rivera, A., Benham, T., Casassa, G., Bamber, J., Dowdeswell, J.A., 2007. Ice elevation and areal changes of glaciers from the Northern Patagonia Icefield, Chile. Glob. Planet. Change 59, 126–137.
Schildgen, T.F., Balco, G., Shuster, D.L., 2010. Canyon incision and knickpoint propagation recorded by apatite $^{4}He/^{3}He$ thermochronometry. Earth Planet. Sci. Lett. 293, 377–387.
Shuster, D.L., Farley, K.A., 2004. $^{4}He/^{3}He$ thermochronometry. Earth Planet. Sci. Lett. 217, 1–17.
Shuster, D.L., Farley, K.A., Sisterson, J.M., Burnett, D.S., 2004. Quantifying the diffusion kinetics and spatial distributions of radiogenic ^{4}He in minerals containing proton-induced ^{3}He. Earth Planet. Sci. Lett. 217, 19–32.
Shuster, D.L., Farley, K.A., 2005. $^{4}He/^{3}He$ thermochronometry: theory, practice, and potential complications. Rev. Mineral. Geochem. 58, 181–203.
Shuster, D.L., Ehlers, T.A., Rusmore, M.E., Farley, K.A., 2005. Rapid glacial erosion at 1.8 Ma revealed by $^{4}He/^{3}He$ thermochronometry. Science 310, 1668–1670.
Shuster, D.L., Flowers, R.M., Farley, K.A., 2006. The influence of natural radiation damage on helium diffusion kinetics in apatite. Earth Planet. Sci. Lett. 249, 148–161.
Shuster, D.L., Cuffey, K.M., Sanders, J.W., Balco, G., 2011. Thermochronometry reveals headward propagation of erosion in an alpine landscape. Science 332, 84–88.
Stüwe, K., Hintermüller, M., 2000. Topography and isotherms revisited: the influence of laterally migrating drainage divides. Earth Planet. Sci. Lett. 184, 287–303.
Thomson, S.N., Brandon, M.T., Tomkin, J.H., Reiners, P.W., Vásquez, C., Wilson, N.J., 2010a. Glaciation as a destructive and constructive control on mountain building. Nature 467, 313–317.
Thomson, S.N., Brandon, M.T., Reiners, P.W., Zattin, M., Isaacson, P.J., Balestrieri, M.L., 2010b. Thermochronologic evidence for orogen-parallel variability in wedge kinematics during extending convergent orogenesis of the northern Apennines, Italy. Geol. Soc. Am. Bull. 122, 1160–1179.
Ton-That, T., Singer, B.S., Mörner, N.A., Rabassa, J., 1999. Datación de lavas basálticas por 40Ar/39Ar y geología glacial de la región del lago Buenos Aires, provincia de Santa Cruz, Argentina. Rev. Asoc. Geol. Argent. 54, 333–352.
Tremblay, M.M., Fox, M., Schmidt, J.L., Tripathy-Lang, A., Wielicki, M.M., Harrison, T.M., Zeitler, P.K., Shuster, D.L., 2015. Erosion in southern Tibet shut down at ∼10 Ma due to enhanced rock uplift within the Himalaya. Proc. Natl. Acad. Sci. 112, 12030–12035.
Valla, P.G., Shuster, D.L., van der Beek, P.A., 2011. Significant increase in relief of the European Alps during mid-Pleistocene glaciations. Nat. Geosci. 4, 688–692.
Yanites, B.J., Ehlers, T.A., 2012. Global climate and tectonic controls on the denudation of glaciated mountains. Earth Planet. Sci. Lett. 325–326, 63–75.